https://doi.org/10.5194/egusphere-2025-4184
Preprint. Discussion started: 28 October 2025

Linking Permafrost Deformation to Active Layer Freeze-thaw Dynamics in the Qinghai-Tibet Engineering Corridor

Xie Hu[1], Yuqi Song[1], Sayyed Mohammad Javad Mirzadeh[1], Qingbai Wu[2], Dongfeng Li[3], Yiling Lin[1], Yuanzhuo Zhou[1], Mei Chen[1], Shengwe Qi[4], Kristy Tiampo[5]

[1]College of Urban and Environmental Sciences, Peking University, Beijing 100871, China
[2]State Key Laboratory of Frozen Soil Engineering, Northwest Institute of Eco-Environment and Resources, Chinese Academy of Sciences, Lanzhou 730000, China
[3]College of Environmental Sciences and Engineering, Peking University, Beijing 100871, China
[4]State Key Laboratory of Lithospheric and Environmental Coevolution, Institute of Geology and Geophysics, Chinese Academy of Sciences, Beijing, China
[5]Cooperative Institute for Research in Environmental Sciences, University of Colorado Boulder, Boulder 80309, USA

Correspondence to: Xie Hu (hu.xie@pku.edu.cn)

Abstract. The Qinghai-Tibet Engineering Corridor (QTEC), traversing hundreds of kilometers of sensitive permafrost, hosts critical lifelines increasingly threatened by climate-induced ground deformation and thermokarst disasters. However, we still lack knowledge about the spatiotemporal characteristics of permafrost states and associated ground deformation at a finer scale. Here we derive ~120-m-resolution surface displacements during 2014-2022 from Sentinel-1 interferometric synthetic aperture radar (InSAR) data processing. We disentangle secular displacement rates from seasonal variations, quantified seasonal amplitudes and timings, and determine displacement directions through complementary ascending and descending observations. Results reveal extensive subsidence throughout the QTEC, exceeding 20 mm/year in areas between Golmud and Nagqu. Seasonal deformation, driven primarily by frost-heave, thaw-settlement cycle of permafrost, can surpass 40-80 mm, with valley floors peaking in spring and hillslopes peaking in autumn due to different hydro-thermal and mechanical responses. Seasonal amplitude of vertical displacements effectively constrains ALT, indicating ALT ≥1 m where seasonal amplitude exceeds 55 mm. With the constraint from in-situ ALT measurements and the assumption of a complete ice melt in the fall, a freeze-thaw density-change model pictures a regional map of ALT at high resolution, where the permafrost to the west of QTEC exhibits a greater ALT compared to the eastern section. Alarming numbers of thermokarst phenomena (18 thaw slumps, 2,812 thaw lakes) within 2 km of critical infrastructure underscore escalating hazards. Our findings emphasize the urgent need for integrated monitoring and adaptive strategies to mitigate intensifying risks from permafrost degradation across the QTEC.

https://doi.org/10.5194/egusphere-2025-4184
Preprint. Discussion started: 28 October 2025

1 Introduction

The Qinghai-Tibet Engineering Corridor (QTEC) serves as the "Sky Road" linking Tibet (Xizang) to the rest of China, home to critical infrastructure, i.e., the Qinghai-Tibet highway and railway systems, the Golmud-Lhasa pipeline, the Lanzhou-Xining-Lhasa optical cable, and a power transmission line (Jin et al., 2008). The climate change-driven ground deformation and thermokarst disasters are prevalent in QTEC, where the Golmud–Lhasa railway spans 1,124 km, with 448 km built atop the permafrost (Fig. 1). Permafrost is characterized by soil or rock that maintains a temperature at or below 0°C for a minimum of two consecutive years. Frozen soil can be classified into three types: short-term frozen soil (lasting hours to weeks), seasonal frozen soil (with monthly changes), and permafrost (remaining frozen for years to millennia). A defining feature of permafrost is the active layer, a seasonally thawed soil layer that melts downward in summer and freezes bidirectionally in winter. This layer is essential for water and heat exchange between the ground and atmosphere. The active layer thickness (ALT) is recognized as one of the 55 Essential Climate Variables by the Global Climate Observing System for monitoring permafrost conditions.

Qinghai-Tibet Plateau (QTP) has experienced a rise in air temperature of about 0.4 °C per decade (e.g., Ran et al., 2018). This increase has resulted in the degradation of permafrost, as revealed by the ice melt and permafrost shrinkage. ALT increases at a rate of 195 mm per decade from 1980 to 2018 according to borehole measurements (Zhao et al., 2020). Consequently, the melted sediments are compacted and settled due to the gravity, and the elevated pore water pressure generated during this process facilitates the displacement of the soil materials (French, 2007; Nelson et al., 2001). In the regions with significant permafrost degradation and ground displacement, the thermokarst hazards such as thermokarst settlement/thermokarst subsidence, thaw slumps, and thermokarst/thaw lakes could be triggered. The seasonal frost heaving and thaw subsidence process within the active layer also leads to the periodic ground deformation, destabilizing the permafrost environment. The joint impacts of land subsidence resulting from the melting of underground ice, the seasonal deformation due to active layer frost-heave, thaw-settlement cycle, and the emergence of thermokarst disasters, damage the residential buildings, roadbeds, and bridges in the permafrost regions. This situation presents substantial risks to the transportation safety of QTEC (Hjort et al., 2022; Yu et al., 2013).

The permafrost environment, characterized by its fragility and spatial-temporal heterogeneity, requires precise and high-resolution observations to effectively monitor its dynamic changes. While field observations (e.g., temperature and soil moisture measurements, Global Navigation Satellite System (GNSS) for surface displacement, and ground-penetrating radar for ALT measurements) deliver accurate permafrost status at isolated site, they are labor-intensive and spatially limited across the QTP. Remote sensing, particularly Synthetic Aperture Radar (SAR), overcomes these constraints with large-scale coverage, frequent revisits, and all-weather operability. Time-series interferometric SAR (InSAR) further enables the systematic detection of surface deformation at a regional scale. Notably, InSAR-derived displacement patterns directly reflect

https://doi.org/10.5194/egusphere-2025-4184
Preprint. Discussion started: 28 October 2025

permafrost dynamics, including long-term degradation and seasonal frost heave and thaw subsidence, serving as important indicators of environmental conditions in these fragile regions (Liu et al., 2010).

Studies employing time-series InSAR have revealed distinct displacement patterns in permafrost regions of the QTP. For example, Daout et al. (2017) observed limited seasonal ground movement (0 to 12 mm) in a 60,000 km^2 area in northwestern Tibet using ENVISAT images covering 2003 to 2011, attributing reduced amplitudes to the arid climate and thermal constraints. Reinosch et al. (2020) identified complex surface displacement dynamics in the Nam Co area using Sentinel-1 images from 2014 to 2018 and reported that the flat terrain exhibited strong seasonal vertical oscillations (5-10 mm) driven by frost-heave, thaw-settlement cycle of active layer, while unstable slopes demonstrated both seasonal deformation and downslope movements (8-17 mm/yr). Chen et al. (2022) documented linear subsidence (up to 20 mm/yr) and pronounced seasonal deformation (up to 80 mm with an average of ~10 mm) in the vast regions (~140,000 km^2) of central QTP by integrating Sentinel-1 images and MODIS land surface temperature products (2014-2019), linking higher subsidence to ice-rich, warmer permafrost and seasonal fluctuations to gentle terrain. Lu et al. (2023) detected pervasive permafrost degradation in Hoh Xil using Sentinel-1 images from 2015 to 2020, characterized by subsidence rate faster than 2 mm/yr in flat zones and thermokarst features. Collectively, these findings underscore spatially heterogeneous displacement governed by climate, topography, ground ice content, and thermal regimes.

Frost heave and thaw settlement in permafrost regions are governed by ice-water phase changes in the active layer, enabling InSAR-derived surface displacement to estimate ALT at high spatial resolutions. Wang et al. (2018) linked surface subsidence to active layer ice-water phase changes using TerraSAR-X data collected between 2014 and 2016 in Beiluhe region, modeling ALT variations across land cover types via deformation and groundwater content. Similarly, Zhang et al. (2020) integrated Sentinel-1 seasonal displacement (up to ~60 mm) with soil moisture profiles across the Tuotuohe-Wudaoliang region, estimating a mean active layer thickness (ALT) of 1.62 m in alpine meadow areas and 2.9 m in alpine desert zones, aligned with field observations. Li et al. (2023) refined ALT modeling by incorporating unfrozen water dynamics and two-dimensional ground deformation from InSAR time series. Beyond approaches based on ice-water volume change, ALT can also be inferred through the thermal properties of soils, utilizing the temporal lag between maximum thaw settlement and peak air temperature (Li et al., 2015). The existing studies on permafrost deformation retrieval and deformation-based ALT estimation focus on small study areas or short temporal elapses.

In this study, we utilize ascending and descending satellite observations from the Copernicus Sentinel-1 mission to produce ground displacements at a ~120-meter resolution across the QTEC during 2014–2022, including the secular (long-term) trends, seasonal amplitudes, and phase timings. We further infer the direction of ground displacements by evaluating the consistency between ascending and descending line-of-sight observations. The drivers of the ground deformation are elucidated through analyzing the relationship between ground displacements and hydro-thermal characteristics of permafrost such as ground

https://doi.org/10.5194/egusphere-2025-4184
Preprint. Discussion started: 28 October 2025

temperature. We also use seasonal vertical displacement amplitudes in conjunction with existing ALT interpretations to estimate the lower boundary of ALT. By establishing an illustrative theory of water density change during freeze–thaw transitions, allowing for unfrozen water existence in freeze season, and assuming a complete water melt in the active layer during thaw, we derive high-resolution ALT estimates cross QTEC. In addition to displacement analysis, we perform a statistical assessment of representative thermokarst-related hazards along the QTEC. These findings can help better plan for the infrastructure construction and anthropogenic activities in the QTEC and supporting adaptative strategies in response to ongoing climate change.

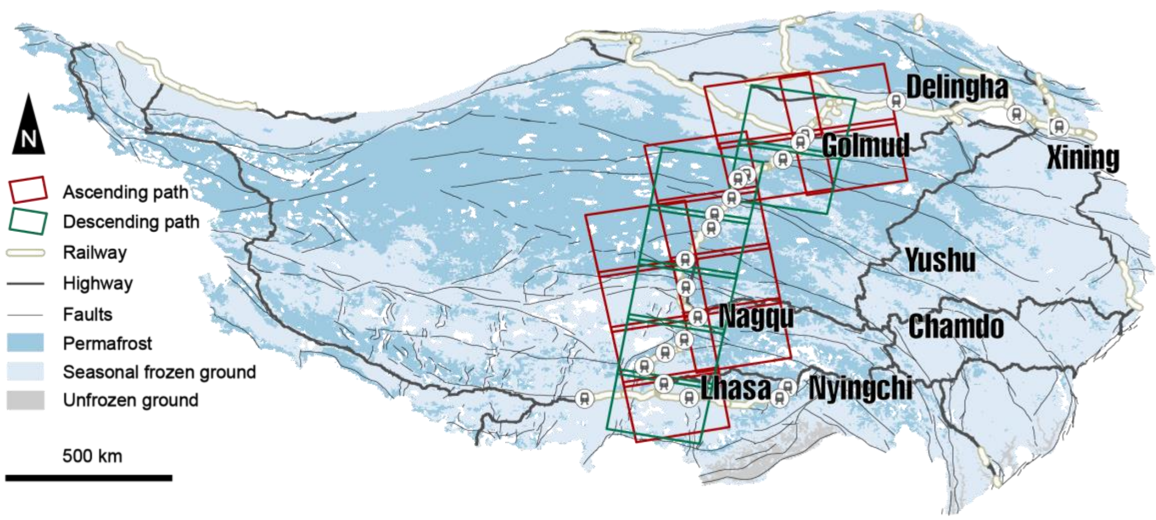

Figure 1: Landscape of Qinghai-Tibet Plateau (QTP). Red and green boxes show the footprints of Sentinel-1 ascending and descending frames, respectively, covering the Lhasa to Golmud section of the Qinghai-Tibet transportation corridor including the railway and highway systems. The permafrost distribution map is sourced from Zou et al. (2017).

2 Methods

2.1 Time-series InSAR analysis

In this study, we apply time-series InSAR analysis to measure the ground deformation across the QTEC. As an active microwave sensor, SAR has the unique advantage of penetrating clouds and rains. InSAR obtains digital elevation models and surface deformation by calculating the phase difference between two SAR images (Lu and Dzurisin, 2014). Since the introduction of Persistent Scatterer Interferometry (PSInSAR) (Ferretti et al., 2001) and Small Baseline Subset (SBAS) (Berardino et al., 2002), time series InSAR analysis technology has continuously derived new methods, but the core of time series analysis, regardless of the proposed names, is the least-squares estimations based on a collection of interferograms. When the interferogram network is not connected, the singular value decomposition can be performed on the subset to obtain the time series change of the phase, which is then converted into the time series deformation.

https://doi.org/10.5194/egusphere-2025-4184
Preprint. Discussion started: 28 October 2025

We collected 5,440 Sentinel-1 images acquired from December 2014 to September 2022 in Interferometric Wide swath (IW) mode, covering 12 frames from 4 ascending tracks (460,456 km^2) and 7 frames from 2 descending tracks (298,068 km^2). We utilized the InSAR Computing Environment (ISCE) software to generate 17,987 interferograms with temporal intervals ranging from 12 to 60 days (the maximum interval extended up to 216 days during periods of lower image acquisition frequencies) and applied multilook numbers of 8 in azimuth and 40 in range, resulting in a spatial resolution of ~120 m. The topographic phase was eliminated using the 30-m-resolution shuttle radar topography mission (SRTM) DEM, and phase values were unwrapped using the statistical-cost network-flow algorithm for phase unwrapping (SNAPHU). We used the Miami InSAR time-series software in Python (MintPy) to conduct time series analyses (Zhang et al., 2019). An average spatial coherence threshold of 0.6 (for areas with sufficient high-quality interferograms) or 0.45 (for areas with insufficient interferograms to construct a robust network) was adopted to remove outliers affected by unwrapping errors and decorrelation. The Python based atmospheric phase screen estimation (PyAPS) and the ECMWF reanalysis v5 (ERA-5) weather model with a spatial resolution of 31 km were utilized to correct tropospheric delays (Jolivet et al., 2011). Phase ramps caused by the residual long-wavelength tropospheric and ionospheric delays, as well as orbital errors, were further removed by calculating a linear ramp at each epoch. Pixels with temporal coherence lower than 0.6 were masked out to ensure a reliable network inversion. InSAR baseline networks for ascending and descending tracks are shown in Figures S1 and S2, respectively.

2.2 Vertical/horizontal displacement characterization

SAR satellites traverse near both poles during their orbital paths around the Earth. The side-looking imaging system leads to responsive InSAR measurements to the sides, while showing the least sensitivity to the traveling directions. Like many SAR satellites that have been decommissioned or are currently in use, Sentinel-1 exclusively offers a right-side-looking capability. As a result, the ascending and descending InSAR measurements are most sensitive to vertical movements, moderately sensitive to east-west movements, and in limited sensitivity to north-south movements.

Nonetheless, the fundamental limitation of SAR satellite geometry serves as a significant indicator of motion direction (Hu et al., 2021). Specifically, when the ascending and descending InSAR measurements exhibit similar characteristics, the related features predominantly manifest in the vertical direction. Conversely, if the features differ, they mainly occur in the horizontal direction. For example, when the magnitude and sign of secular rates are the same from both the ascending and descending orbits, the ground target primarily moves in a vertical direction. If the slant range increases in both orbits, the target subsides vertically; if the slant range decreases in both orbits, the target uplifts vertically. When the secular rates from both orbits are identical in magnitude but differ in sign, the target may primarily move in the east-west direction. However, if the rates vary between ascending and descending orbits, the direction of the secular movement becomes indeterminate. As for the seasonal variations, when the seasonal amplitude and timing align in both ascending and descending results, the target exhibits seasonal movement in the vertical direction. Conversely, if these factors differ, horizontal seasonal movements become significant. In

https://doi.org/10.5194/egusphere-2025-4184
Preprint. Discussion started: 28 October 2025

cases where the seasonal amplitude measurements from ascending and descending orbits are similar, but the timing is 180° out of phase, the primary motion occurs in the east-west direction. However, when the seasonal amplitude from two orbits differs, it becomes challenging to define the direction of the movements. The time-series InSAR method has an uncertainty of approximately a few millimeters per year. Considering that both annual and seasonal displacement amplitudes can reach several tens of millimeters in QTP, we establish a threshold of 5 mm/year for the secular rate and a threshold of 5 mm for the seasonal amplitude to assess the similarity between ascending and descending results. Moreover, we set a threshold of ±30 days and 180±30 days to evaluate whether the seasonal timing of the ground's peak from the ascending and descending results is in phase or 180° out of phase.

Table 1: Implications from ascending and descending SAR satellites' line-of-sight measurements.

	Secular rates		Implications for the direction of the motions
	Magnitude	Sign	
Ascending/ Descending	Similar	Same	Vertical
	Similar	Opposite	East-west
	Different	\	Undetermined
	Seasonal movements		**Implications for the direction of the motions**
	Amplitude	**Timing**	
Ascending/ Descending	Similar	In-phase	Vertical
	Similar	180° out-of-phase	East-west
	Similar	Others	Undetermined
	Different	\	Undetermined

2.3 Time-series displacement decomposition

We disentangle the InSAR-measured ground deformation with a linear function alongside one or more trigonometric functions, to capture both the long-term deformation trend due to permafrost degradation and ice melt, and seasonal deformation due to frost-heave, thaw-settlement cycle of active layer, respectively. Some research has focused solely on SAR images captured during the permafrost thawing season to generate interferometric pairs (e.g., Chen et al., 2020; Rouyet et al., 2019; Rudy et al., 2018): Thereafter, the average seasonal deformation amplitude for those years can be solved by combining interferometric pairs from several melting seasons, and the long-term deformation trend was identified by forming interferometric pairs from images taken during the same period in consecutive years. On the other hand, some research directly utilizes all SAR images from the study period (e.g., Chen et al., 2022; Daout et al., 2017; Reinosch et al., 2020): the complete deformation sequence was generated by time series InSAR analysis, followed by the extraction of long-term deformation trends and seasonal components, either year by year or through the entire time span. The limitation of these studies stems from the subjective assumption that all ground targets tend to move seasonally.

https://doi.org/10.5194/egusphere-2025-4184
Preprint. Discussion started: 28 October 2025

To be more comprehensive, we evaluate the presence of seasonality for each individual pixel. First, we fit a linear function to capture the long-term trend of the ground deformation and separate the detrended seasonal displacement time series. Then, we apply three independent sinusoidal functions to fit the detrended displacement time series, capturing its first-order variation. It worth noting that the choice of three sinusoidal functions is not arbitrary, because the utilization of more than three sinusoidal functions will potentially capture the high-frequency noise, while less than three sinusoidal functions might be unable to represent the variations present. Subsequently, we identify and tally the peaks and troughs of the seasonal deformation. Typically, one calendar year holds one peak and one trough. This allows us to compile a collection of pixels with an anticipated number of peaks and troughs. Here we adjust this threshold to account for uncertainties, resulting in a range of 16±2 peaks/troughs through 2014 to 2022.

For the pixels exhibiting seasonality, a trigonometric function is employed to disentangle the deformation time series, allowing for the determination of the seasonal deformation amplitude and timing. Here the choice of a single trigonometric component is to characterize the seasonal timing.

$$d(t) = a\,t + b + A\sin\left(\frac{2\pi}{T}(t+\varphi)\right) \quad (1)$$

where a represents the secular rate, $2 \times |A|$ characterizes the seasonal amplitude. We can also quantify the date in one calendar year when the ground surface reaches the upmost, which we denote as the seasonal timing in this study. This approach has proven effective in California (Hu et al., 2021), where variations in secular rate, seasonal amplitude, and seasonal timing, partly or jointly, illustrate the hydrogeological complexities and heterogenous tectonic regimes present in the region.

https://doi.org/10.5194/egusphere-2025-4184
Preprint. Discussion started: 28 October 2025

2.4 Active layer thickness (ALT) retrieval

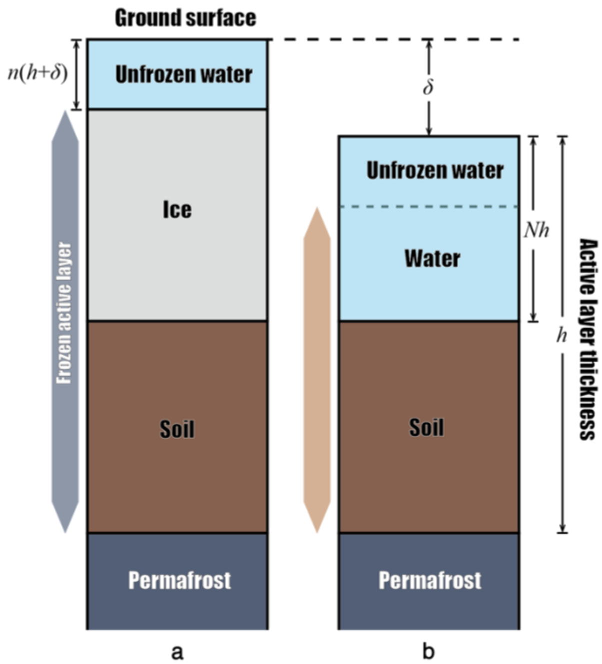

195 **Figure 2: Schematic view of permafrost frost-heave to thaw-settlement transition (not to scale). a, freeze season. b, thaw season. Water, ice, and soil blocks are separated to facilitate the math derivation. Vertical gray bars represent the frozen parts of the active layer during the freeze time epoch, and vertical brown bars represent the thaw parts of the active layer during the thaw time epoch. We refer to Liu et al. (2012) and Li et al. (2023) on the design of this schematic view with modifications.**

The phase transitions of water within the active layer of permafrost lead to cyclical changes in volume and ground deformation. The magnitude of seasonal deformation is influenced by the volumetric water content during the peak freeze and thaw periods of the year. Here we consider the likely existence of unfrozen water in the freeze season and assume that the ice contained in the permafrost melts out in the thaw season. In the schematic view (Fig. 2), water, ice, and soil blocks are separated to facilitate the math derivation. Therefore, we can estimate ALT (H) based on the seasonal amplitude of the vertical displacement δ from the projection of the radar's line-of-sight measurements.

$$H = \frac{\rho_i + n(\rho_w - \rho_i)}{(N - n)(\rho_w - \rho_i)}\delta \quad (2)$$

where ρ_w and ρ_i are the density of water and ice, and here we apply 1,000 and 917 kg/m^3 respectively; n and N are the volumetric water content in dry frozen and wet thaw conditions, respectively. Here we assume that the soil moisture in October, when the land surfaces reach the lowest, represents the volumetric water content during the wet thaw condition (N). Launched in 2015, the Soil Moisture Active Passive (SMAP) mission provides a global-scale soil moisture monitoring approach through its L-band radar (operation ceased in early 2015) and L-band radiometer (operational to date). This study employs the SMAP's Level 4 "root zone" (0-100 cm) soil moisture across the QTEC region. Monthly average soil moisture in QTEC from 2016 to 2022 were acquired via the Google Earth Engine platform, incorporating data at 3-hourly and 9-km resolution. Nonetheless,

https://doi.org/10.5194/egusphere-2025-4184
Preprint. Discussion started: 28 October 2025

due to snow cover, the volumetric water content in dry frozen condition (n) can hardly be observed directly (Du et al., 2025), and it is not viable to be represented by the soil moisture products from SMAP. Previous studies (e.g., Li et al., 2023; Zhang and Wu, 2012) applied a constant 5%. Here we fully utilized a limited number of in-situ ALT measurements in QTEC, constrained n at those sites where all other parameters are available (Eq. 2; Table S1). We used the Spline interpolation to generate a map of n after removing anomalies. Thereafter, we computed the ALT at the same resolution of the input seasonal displacement amplitude (Eq. 2). Although this workflow involves uncertainties originated from parameters themselves in the dry QTP environment, the derivation of ALT is based on physical processes, instead of data-driven machine learning.

3 Results

3.1 Radar's line-of-sight (LOS) displacements

Land subsidence is widespread in the QTEC region, with rates ranging from a few to over 20 millimeters per annum, particularly prominent between Yuzhufeng and Nagqu. In contrast, the regions from south of Nagqu to Lhasa, and the regions to the north of Yuzhufeng railway station are relative stable. Three circular deforming zones in the northernmost of the imaging footprints represent drastic subsidence (radar slant range increase) due to oil/gas extraction in Sanhu depression, Qaidam Basin (Arrow in Fig. 3a). Notably, seasonal displacements clearly cease at the boundary between permafrost regions to seasonally frozen ground regions. We believe that the seasonal deformation of the active layer of permafrost is significant. In contrast, the seasonal frozen soil comprises only a minor portion of the soil mass undergoing phase changes in water, resulting in less noticeable seasonal deformation. Additionally, areas experiencing significant secular subsidence also display pronounced seasonal displacement amplitudes of 40-80 mm, with peak ground elevation typically occurring in spring. The occurrence of relatively large subsidence rates and large seasonal displacement amplitude is likely linked. As permafrost rapidly degrades, increased ice melt causes greater volume loss and faster subsidence, while thickened active layer from the transition of permafrost leads to amplified seasonal ground movements.

Referring to the time-series InSAR observations elsewhere (e.g., Utah, California, and Texas; Hu et al., 2018; Hu et al., 2020; Hu et al., 2021; Qu et al., 2023), linear discontinuities in the secular, seasonal amplitude, and timing of surface displacement fields align with fault strands, the transition zones between sediment-filled basins and bedrock-dominated ranges, and the peripheries of principal aquifers. These patterns suggest groundwater flow disruptions, variations in elastic properties, and the presence of heterogeneous hydrological units. In our study area, several east-to-northeast trending fault strands intersect the QTEC. Notably, the discontinuity in secular displacement aligns with the East Kunlun Fault north of our study area, between Yuzhufeng and Chumaerhe railway stations (Fig. 3a).

https://doi.org/10.5194/egusphere-2025-4184
Preprint. Discussion started: 28 October 2025

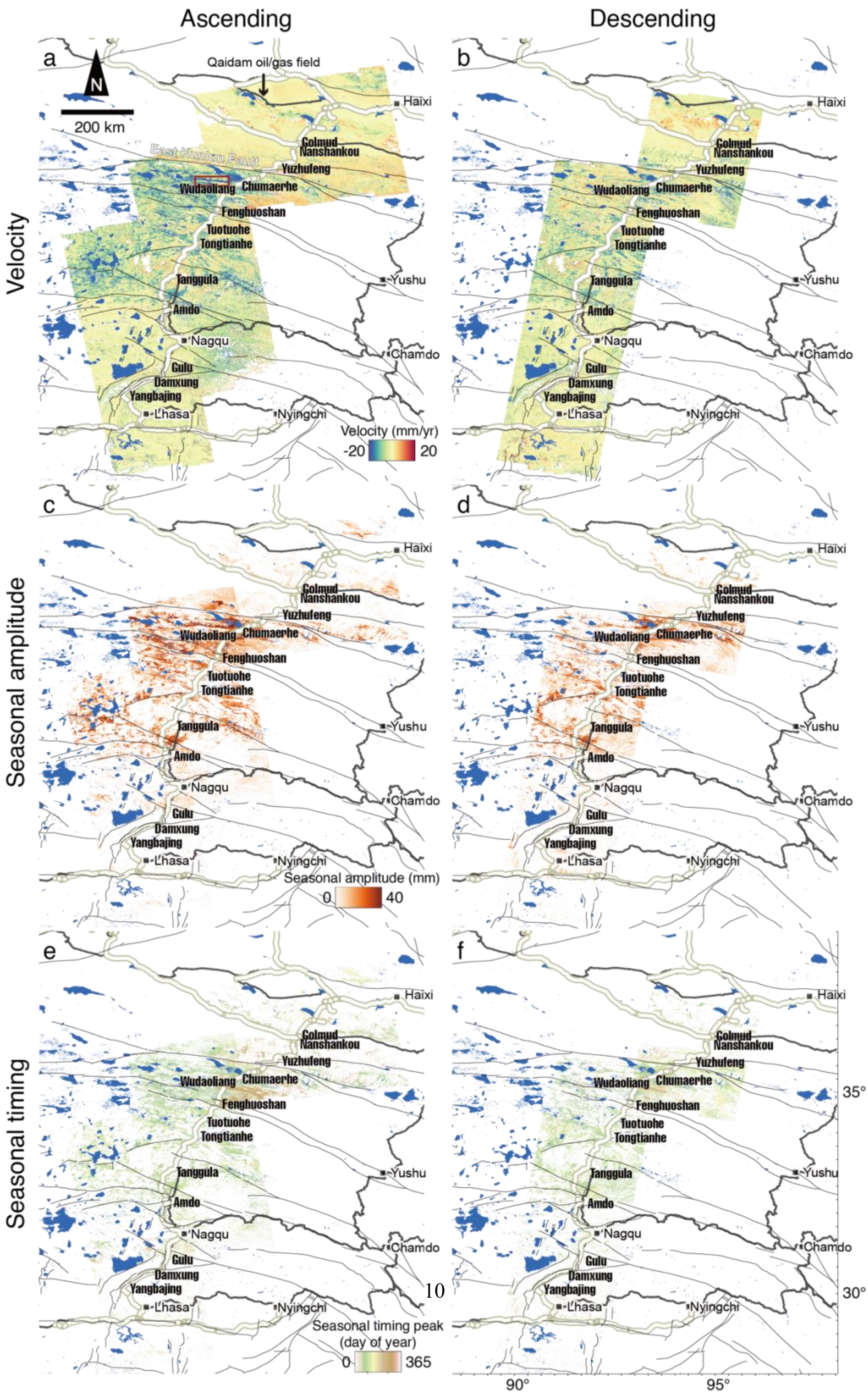

https://doi.org/10.5194/egusphere-2025-4184
Preprint. Discussion started: 28 October 2025

Figure 3: Ground deformation decomposition, all measured in the radar line-of-sight directions. a and b show the secular displacement velocity in mm/yr. The red box in panel a highlight the geographic area located to the west of the railway and highways in Wudaoliang, which will be further detailed in Fig. 4. c and d show the peak-to-trough seasonal displacement amplitude in mm. e and f show seasonal timing (day) when the ground reach the upmost (peak) in one calendar year. a, c, and e show the Sentinel-1 ascending results, while b, d, and f show the Sentinel-1 descending results.

Owing to the high resolution of our displacement products, we identified multiple elongated belts exhibiting distinct secular rates and seasonal amplitudes, often corresponding to topographic transitions (Fig. 4). This anomaly is consistently observed in both ascending and descending measurements, highlighting localized permafrost dynamics distinct from the broader regional patterns. The displacements are more pronounced in the valley floor. These features might not be linked to blind faults, as tectonic motion is less likely to be concentrated within such narrow belts and correlates with the watershed morphology (Fig. 4). Instead, here the large displacements may result from variations in the volume of ground ice and the thermal conditions. Furthermore, the secular rate maps highlight several clusters of active mass-wasting processes (arrows in Fig. 4a, b). The contrasting displacement signs observed in ascending and descending results suggest predominantly horizontal ground deformation in the east-west direction, aligning with slope aspects. Moreover, the seasonal timing also presents significant difference across regions of topographic transition. The hummocky hills reach their highest surface position in the late summer (brownish color in Figs. 3e, f and 4e, f). On consolidated hillslopes, elastic unloading peaks in late summer when substantial meltwater drainage occurs, thereby leading to the peak surface position (Hu et al., 2021). In contrast, the highest surface position for most of the flat areas occurs in spring (greenish color in Figs. 3e, f and 4e, f), when the underlying water/ice-rich layer reaches its most frozen state (see section 4.1 for details).

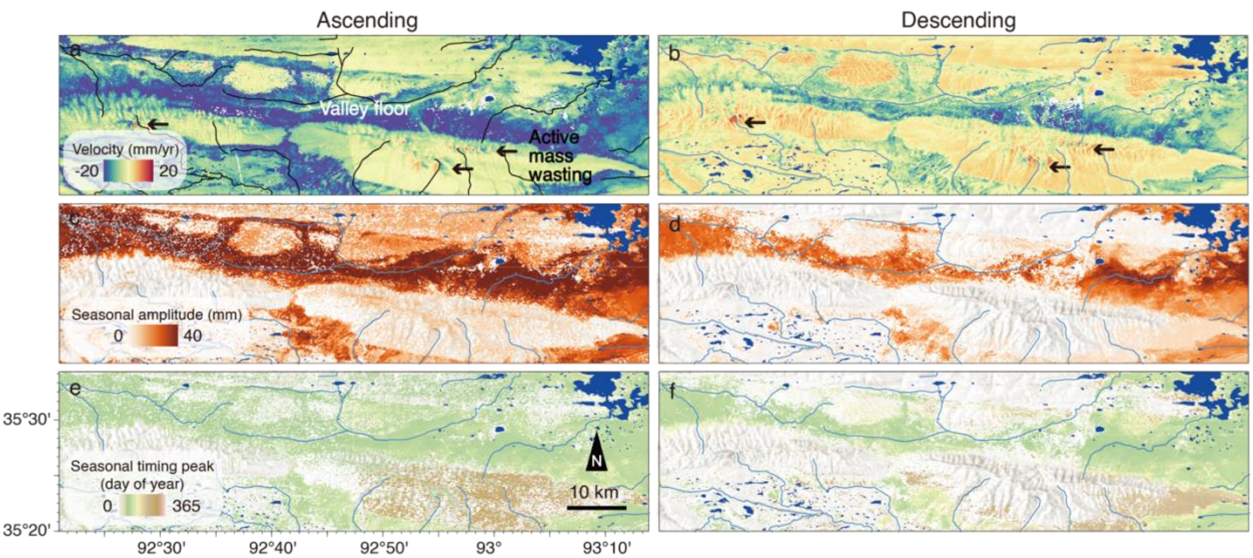

Figure 4: Enlarged ground deformation decomposition results around Wudaoliang (the red box in Fig. 3a). a and b show the secular displacement velocity from ascending and descending results, respectively. c and d show the peak-to-trough seasonal displacement

https://doi.org/10.5194/egusphere-2025-4184
Preprint. Discussion started: 28 October 2025

amplitude from ascending and descending results, respectively. e and f show seasonal timing (day) when the ground reaches the upmost (peak) in one calendar year ascending and descending results, respectively.

3.2 Disentanglement of ground deformation

It is essential to understand that spaceborne line-of-sight measurements represent real movements but do not precisely indicate specific dimensions within three-dimensional Cartesian coordinates. Additionally, spaceborne InSAR is not suitable for capturing predominantly north-south movements without constraints or assumptions (Zheng et al., 2023). Nonetheless, based on the theory and methods we proposed in section 2.3 (Table 1), we conduct non-traditional interpretations of secular and seasonal displacement directions of the entire QTEC. In terms of secular displacement, a total of 6,796,293 out of 11,063,313 pixels (31%) exhibit comparable magnitudes of secular displacement velocities from both ascending and descending orbits, indicating a secular vertical displacement (Fig. 5a). Another 4,267,020 pixels (19%) demonstrate similar magnitudes of secular displacement velocities while contrasting signs from these orbits, pointing to a secular east-west displacement. The pixels with horizontal secular displacement are generally concentrated around the lakes or in the seasonal frozen ground regions around Lhasa and north of Golmud. The remaining 50% of the pixels have an undetermined direction regarding secular displacement. In terms of seasonal displacement, 1,112,335 out of 2,762,425 pixels (40%) display similar amplitudes and in-phase timing, suggesting vertical variations and they are more frequent over the permafrost area around Chumaerhe and to the south of Fenghuoshan (Fig. 6). The east-west seasonal displacement can rarely be seen in our study area. Only 8,489 pixels (<1%) show similar amplitudes but with a 180° out-of-phase timing, indicating east-west displacement. The remaining 240,888 (9%) exhibit a similar amplitude with other timing situations, and 1,400,713 (51%) pixels present different amplitudes from ascending and descending results, suggesting an undetermined direction for seasonal displacement.

https://doi.org/10.5194/egusphere-2025-4184
Preprint. Discussion started: 28 October 2025

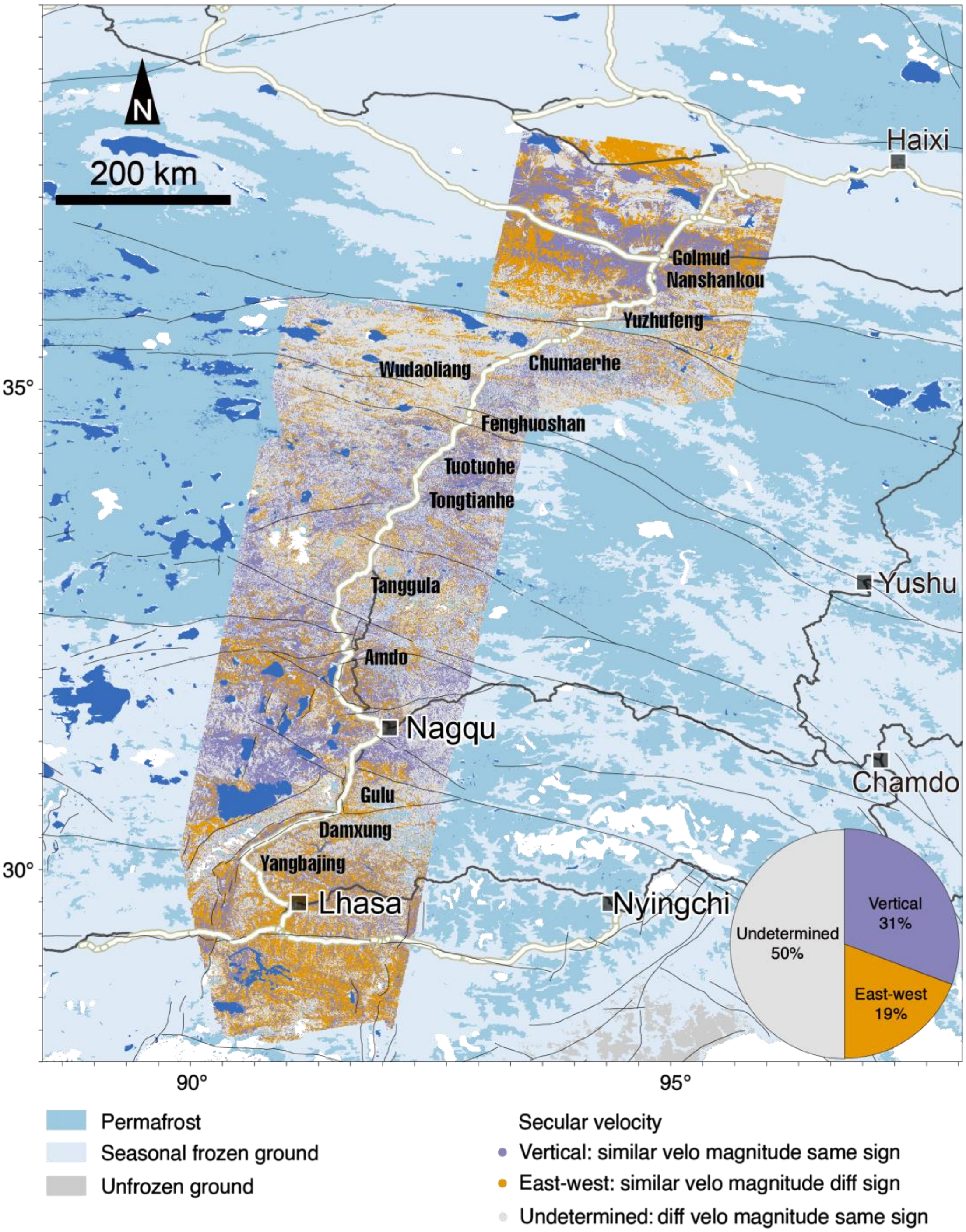

Figure 5: The inferred direction of motion of the secular velocity. Pixels in various colors represent secular displacement, indicating different directions. The pie chart illustrates the percentage of the corresponding inferred secular displacement directions.

https://doi.org/10.5194/egusphere-2025-4184
Preprint. Discussion started: 28 October 2025

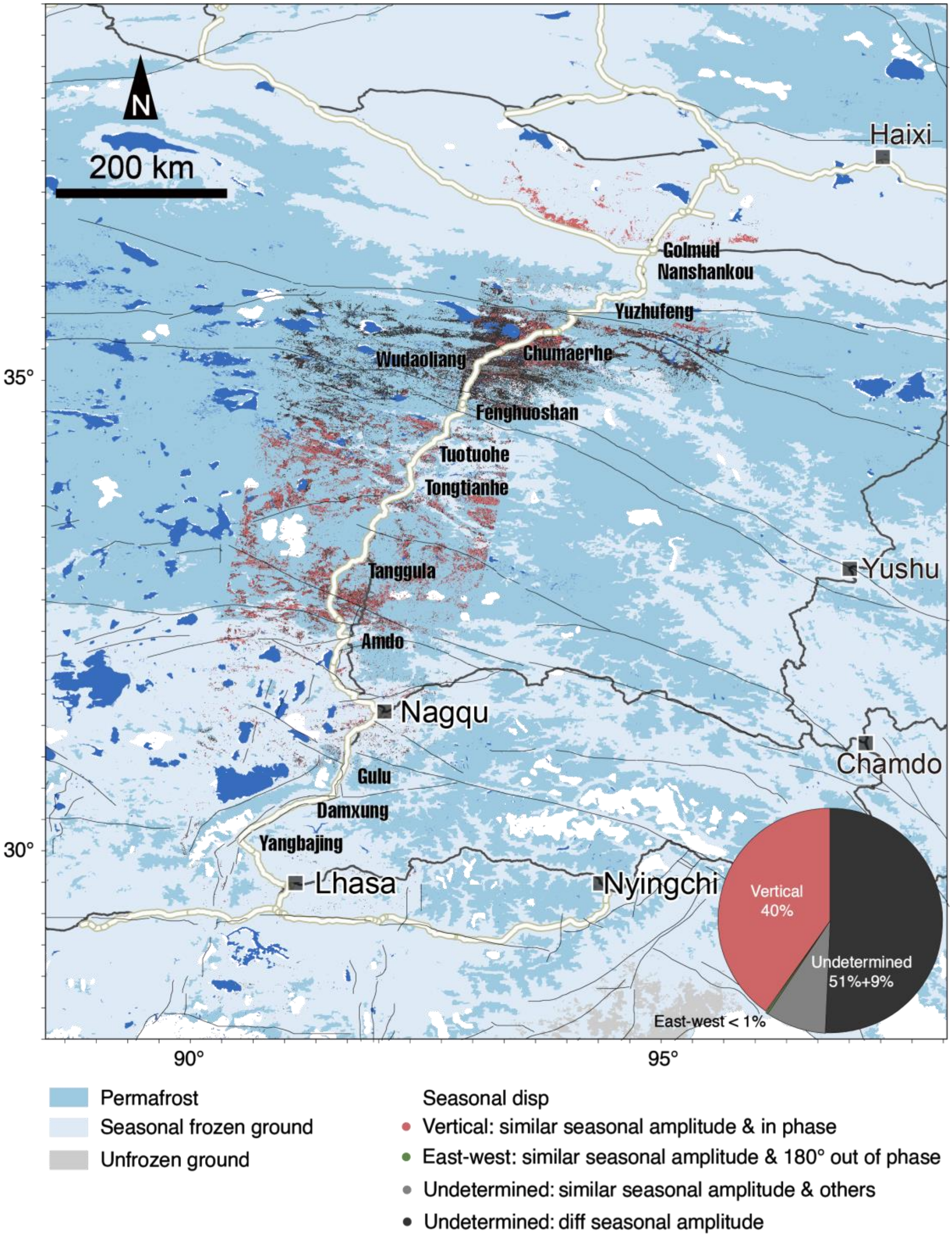

Figure 6: The inferred direction of motion of the seasonal displacement. Pixels in various colors represent seasonal displacement, indicating different directions. The pie chart illustrates the percentage of the corresponding inferred directions of seasonal displacement.

https://doi.org/10.5194/egusphere-2025-4184
Preprint. Discussion started: 28 October 2025

4 Discussion

4.1 Hydrological and climatic drivers for the seasonal ground deformation of permafrost

In areas where the seasonal amplitude of ground deformation is pronounced, the cross-correlation between ground deformation and ground temperature time series is often significant. We investigate the pixels exhibiting the greatest seasonal ground deformation amplitudes (exceeding 80 mm) in both ascending and descending line-of-sight observations and find that the selected pixels are in close proximity to surface water (pentagons in Fig. 7a, b). The pixel with greatest seasonal ground deformation in ascending results bounds the Yagen Lake, and that in the descending results is in a river valley featured with small lakes and braided rivers. Ground temperature over the upper 2 meters of soil at the locations of the selected pixels is available from the publicly free GLDAS dataset, displays clear seasonal fluctuations. The ground temperature typically ranges from about 260 K (-13.15 °C) to 280 K (6.85 °C), with the period when temperatures exceeding (273.15 K) 0 °C—indicative of thaw conditions—for roughly half the year from May to October. The displacement time series of the two selected pixels reveal both episodic and gradual subsidence, with cumulative LOS displacement reaching approximately -200 mm over the 2015-2022 period in the ascending results (Fig. 7c).

A clear seasonal variation in both ground deformation (gray lines) and ground temperature (blue lines) for the selected pixels can be drawn from Fig. 7c, with a notable inverse correlation between the two variables in both ascending and descending results. Land subsidence typically begins in spring when ground temperature rises to slightly below 0 °C (blue dashed lines in Fig. 7c, d), initiating ground ice thaw and a reduction in soil volume. Conversely, ground uplift tends to occur as temperatures fall to around 0 °C in fall, signaling the onset of freezing and subsequent volumetric expansion. At the selected sites with pronounced seasonal deformation, the peaks in ground deformation generally lag behind the annual minimum ground temperature by approximately four months, reflecting the time required for hydro-thermal alterations. To be specific, the temperature variation at greater soil depths typically responds to changes in air and shallow ground temperatures with a time delay. This thermal lag may explain why the deformation at surface often occurs later than the temperature fluctuations. For instance, in-situ observations from a permafrost station (named TGL) show that the minimum temperature at shallow depths occurs in January, whereas the lowest temperature at deeper levels is not reached until March (Zhao et al., 2022). This temporal pattern is consistent across both ascending and descending radar line-of-sight perspectives, affirming its physical origin rather than being an artifact of satellite geometry. In summary, our results demonstrate a strong seasonal coupling between ground temperature and displacement, likely driven by temperature-dependent freeze and thaw cycle of ground ice within active layer.

https://doi.org/10.5194/egusphere-2025-4184
Preprint. Discussion started: 28 October 2025

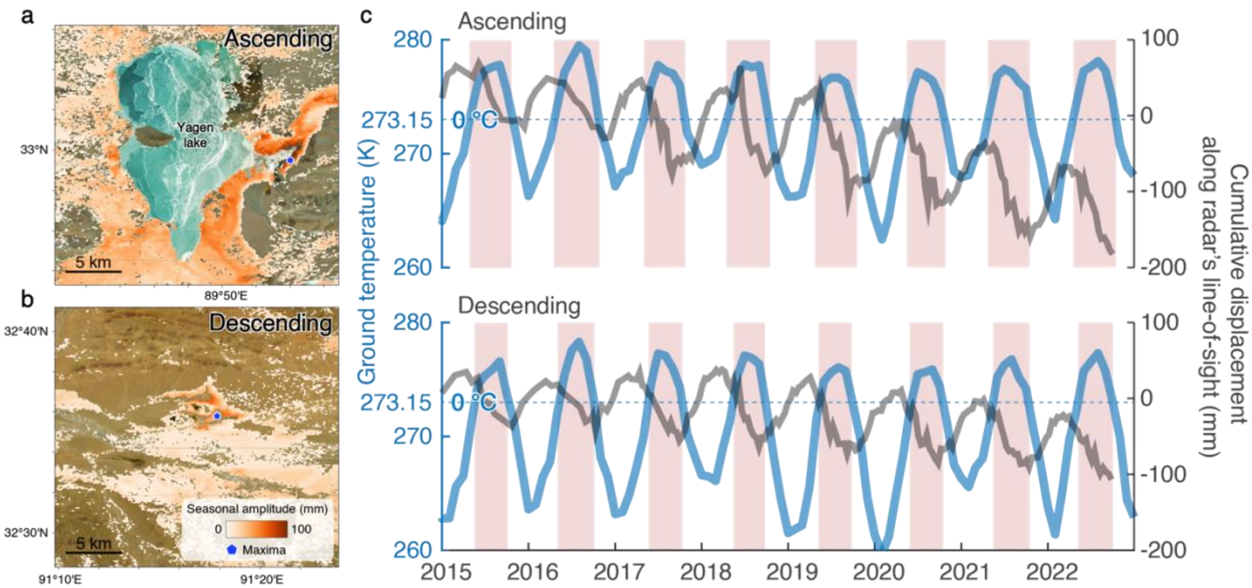

Figure 7: The relationship between seasonal displacements and ground temperature. a and b, areas containing the most pronounced seasonal amplitude of ground displacements from ascending and descending observations, respectively. The maxima of seasonal amplitude are denoted by blue pentagon. c, time series of ground temperature in Kelvin (blue lines, left y-axis) and cumulative displacement along the radar's line-of-sight in millimeters (gray lines, right y-axis) from 2015 to 2022. Blue dashed lines indicate 0 °C. Red bars represent time windows above 0 °C.

4.2 Implications for quantifying the active layer thickness

Since the 1990s, the Qinghai-Tibet Plateau Cryosphere Research Station, operated by the Chinese Academy of Sciences, has initiated the establishment of active layer observation sites along the QTEC (Zhao et al., 2021). While the most fundamental method for quantifying active layer thickness involves extracting stratigraphic profiles during field measurements, this approach, which relies on in-situ data collection, can only capture frozen soil deformation and active layer thickness parameters at a limited number of isolated locations, often constrained by accessibility. For example, the monitoring stations are clustered in the QTEC in the eastern region, whereas the western areas with low population density have a notable scarcity of stations (Ni et al., 2021). To infer large-scale, seamless ALT, assumption-based numerical models and limited-data-driven machine learning approaches have become popular. For example, the Community Surface Dynamics Modeling System (CSDMS) provides the open-source numerical models of permafrost dynamics including ALT and temperature profiles with depth (Overeem et al., 2018). Niu and Yin (2018) relied on GIPL2.0 frozen soil model to synergize temperature, soil types, topography, and in-situ measurements of ALT from 15 sites (33 boreholes were used in Yin et al., 2018 from the same lab) along QTEC to obtain the ALT for the entire area with 1 km spatial resolution, and demonstrated that the ALT is below 2 m in alpine areas, 3 to 4 m in high plain areas, and above 4 m in river valleys; Ni et al. (2021) collected ALT data from 77 sites, air temperature, precipitation, topography, and soil organic matter data to derive the regional ALT at 0.1° resolution based on

https://doi.org/10.5194/egusphere-2025-4184
Preprint. Discussion started: 28 October 2025

statistical and machine learning methods, and the average ALT over QTP is 2.3±0.60 m. ALT estimates from the above two studies show evident disparities.

InSAR-derived time-series displacement provides a solution for quantifying large-scale ALT by leveraging the basic principle of density differences between ice and water. This approach assumes that the seasonal displacement over the permafrost regions is exclusively a result of the phase change of soil water within the active layer (Liu et al., 2012). Seasonal amplitude can serve as an indicator for determining the relative ALT distribution across the space. Drawing on the ALT findings presented by Niu and Yin (2018) and Ni et al. (2021), we investigate the intrinsic relationship between ground deformation and ALT. We compute the vertical displacement from a simple projection of InSAR line-of-sight measurements using the respective incidence angle at each pixel. Overall, the vertical displacements are about 1.17 to 1.46 times of than the InSAR line-of-sight measurements from near range to far range in the image swath.

The relationship between seasonal deformation and ALT varies with soil texture and moisture conditions. Chang et al. (2024) observed differing trends across permafrost environments, notably between the sparsely vegetated, dry soils of the QTP and the densely vegetated, poorly drained soils of the Arctic. Difference in in-situ ALT measurement approaches between these regions may contribute to this uncertainty. In the QTP, ALT is primarily measured using soil sensors, boreholes, and ground-penetrating radar, as primarily implemented by the Cryosphere Research Station of the Chinese Academy of Sciences (e.g., Wu et al., 2012; Zhao et al., 2021). In contrast, Arctic measurements rely on mechanical probing, thaw tubes, and ground temperature interpolation, compiled by the Circumpolar Active Layer Monitoring Network (CALM) (e.g., Brown et al., 2000). Rather than seeking a direct correlation between seasonal deformation and ALT, we highlight a noticeable gap in the lower-right corner of the scatter plots (i.e., high seasonal amplitude of vertical displacement but low ALT; Fig. 8b and c). We therefore focus on the linear relationship between seasonal deformation and the lower bounds of ALT estimates. The linear coefficients differ when applying ALT estimates from these two studies. Additionally, the Y-intercepts exhibit opposite signs, indicating substantial uncertainties in the results. The envelops on the lower limits of the ALT against the seasonal displacement report that the ALT will be no less than ~1 m when the seasonal amplitude of line-of-sight displacement derived from spaceborne InSAR reaches 40 mm, and the inferred seasonal amplitude of vertical displacement reaches 55 mm (Fig. 8b, c).

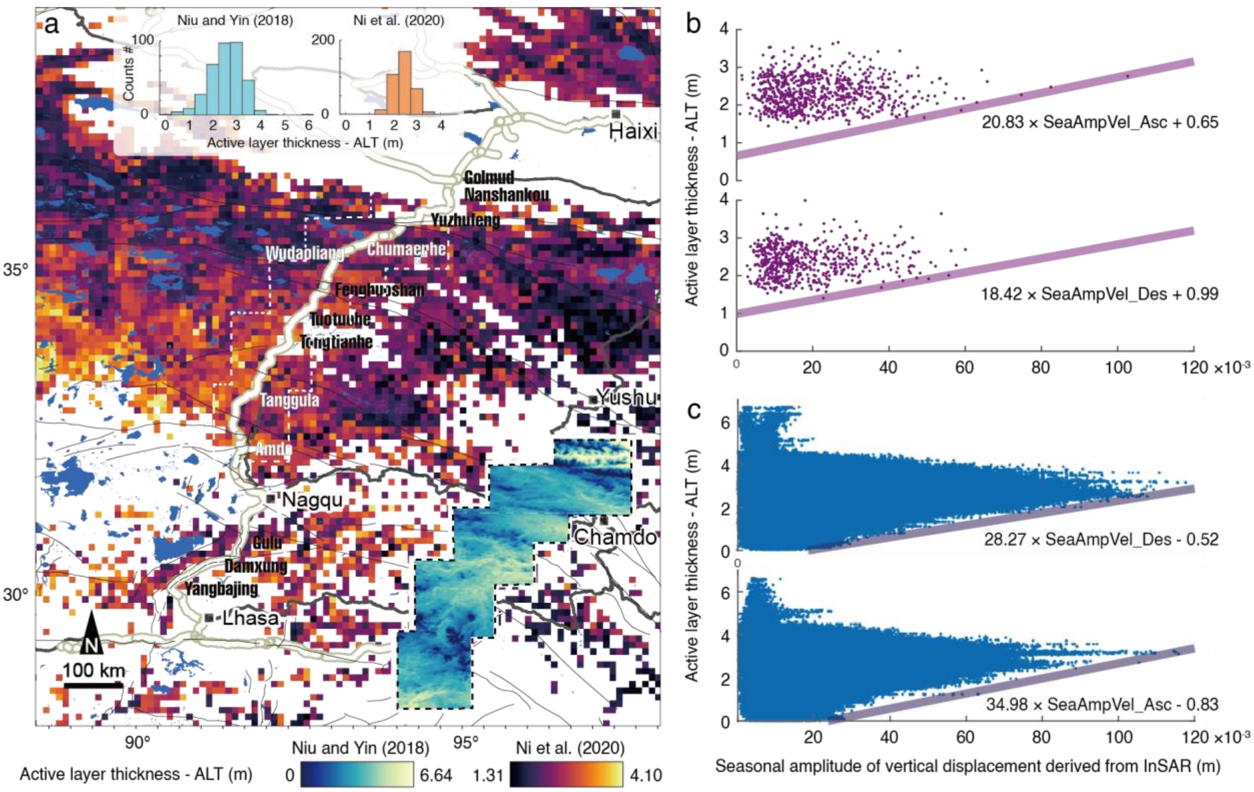

Figure 8: Reported ALT from reading literatures and the relationship with the seasonal ground deformation amplitude. a, ALT over QTEC published as the 10-m-reolution in Niu and Yin (2018) (only available for the QTEC area) and the 0.1° (~10-km)-resolution in Ni et al. (2021). b and c, the relationship between ALT from different sources and the seasonal amplitude of vertical displacement derived from ascending and descending Sentinel-1 InSAR measurements, respectively. Thick lines label the lower bounds of the ALT envelope constrained by the seasonal amplitude.

InSAR-derived seasonal amplitude of vertical displacement and the annual change of volumetric water content allow us to compute large-scale ALT based on equation (3) (Fig. 9). West of QTEC has thicker active layers compared to the east part. The reliability of our method is contingent upon two issues. The first issue stems from the interpolation of the inferred volumetric water content in dry spring from in-situ ALT measurements at discrete sites along the highways (circles in Fig. 9) (Chang et al., 2024 and reference therein), and the interpolation stretching to the external areas inevitably lead to uncertainties. The second issue arises from the volumetric water content in wet fall based on large-scale soil moisture products, which frequently vary across different data sources such as from SMAP and ERA5-Land missions. Nonetheless, our method is robust in achieving large-scale ALT through measurements rather than relying solely on data-driven techniques that lack solid physical foundations.

https://doi.org/10.5194/egusphere-2025-4184
Preprint. Discussion started: 28 October 2025

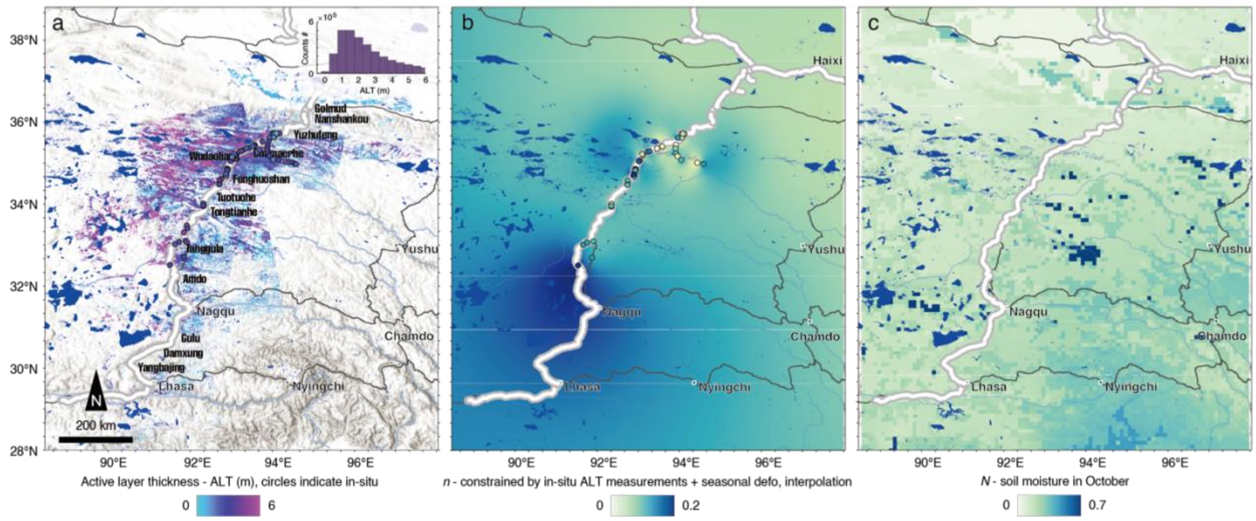

Figure 9: ALT estimates based on seasonal amplitude of vertical displacement derived from InSAR measurements. a, ALT. Inset histogram shows the frequency of ALT in the overlapping area of results from Niu and Yin (2018) and Ni et al. (2021). b, the interpolation results of the volumetric water content in frozen condition (n in Eq. 2), constrained by in-situ ALT measurements (Table S1) and seasonal deformation amplitude (Fig. 3c, d). c, the volumetric water content in thaw condition (N in Eq. 2) represented by soil moisture in October when the land surface reach the lowest.

For a systematic comparison of ALT estimates, we have resampled the estimates to the same geographic locations referring to the resolution of InSAR. Niu and Yin (2018) reported ALT values primarily ranging between 2 and 4 m, with a distribution peak around 3 m and relatively few occurrences below 1.5 m or above 4.5 m (inset in Fig. 8a). Note that we have excluded the negative values. In contrast, Ni et al. (2021) observed a more tightly clustered distribution, predominantly between 2 and 3.5 m, peaking at 2.5-3 m, indicating a narrower spread compared to Niu and Yin (2018). In this study relying on the simple freeze-thaw water density difference and seasonal displacement measurements, the derived ALT minima distribution reflects a skew toward shallower depths and taper off toward higher values (inset in Fig. 9a). This is not a surprise considering the employed seasonal displacement amplitudes are generally small—and larger amplitudes occur less frequently—the resulting ALT shifts toward lower values. Additionally, referring to the modeled ALT from the above-mentioned studies, the seasonal displacement amplitude only indicates the lower bounds of ALT (exemplified in Fig. 8b, c).

Overall, the discrepancies in ALT estimates may be attributed to methodological differences, uncertainties of input features, temporal changes in permafrost conditions—such as those driven by climate warming—or localized environmental controls. The “wiggle” in ALT peaks in the frequency histograms in the past through the future can be used as indicators for evolution of permafrost degradation. Further investigations are warranted to better understand the permafrost spatiotemporal dynamics.

4.3 Thermokarst disasters over the QTEC

Thermokarst disasters can reshape landscapes, alter hydrological regimes, mobilize the sequestered soil organic carbon, and likely amplify climate feedback loops (Bense et al., 2012; Yang et al., 2023, Turetsky et al., 2020; Wang et al., 2020; Mu et al., 2020). Beyond that, thermokarst disasters also pose threats to the QTEC due to the melting of ice-rich permafrost (Niu et al., 2011; Xia et al., 2022; Zhou et al., 2024). Among the various manifestations of these disasters, we focus on thaw slumps (TSs) and thermokarst/thaw lakes (TLs), which have been more extensively documented. Regarding the TS, Luo et al. (2014) conducted a comprehensive field survey in conjunction with the visual interpretation of SPOT-5 remote sensing images, identifying 42 TSs within a 5-km radius on both sides of the Qinghai-Tibet railway. In a subsequent study, Luo et al. (2019) utilized a collection of Landsat images, spanning the years 2008 to 2017, to manually delineate 438 TSs in the Beiluhe area. With advancements in deep learning, semantic segmentation models have emerged as effective tools for extracting the boundaries of TS. In this context, Huang et al. (2020) employed the DeepLabv3+ semantic segmentation model on 3-m-resolution CubeSat PlanetScope images to automate the inventory procedure. Similarly, Xia et al. (2022) identified 875 TSs within the QTEC, with 474 in the Beiluhe region, while 38 were located near highways and railways. Luo et al. (2022a) identified 2,669 active TSs in the QTP using satellite images from Gaofen, Worldview-I, SPOT-5, as well as Google Earth archive, collected during 2018-2020. Lin et al. (2025) documented an increase in the number of TSs in the Beiluhe area from 803 to 885, with the affected area expanding from 1,727 ha to 2,329 ha.

On the QTP, TSs primarily occurred at medium elevations between ~4,600 and 5,000 m in Beiluhe area (Luo et al., 2022a). This is because lower-altitude regions are situated near the lower limits of permafrost, where the underground ice layer is less substantial, making the formation of thaw slumps challenging. Conversely, in higher-altitude areas, temperatures are cooler, allowing the underground ice layer to remain stable, which inhibits melting and the subsequent development of TSs. TSs are predominantly found on gentle slopes ranging from 2° to 10° (Luo et al., 2022a; Mu et al., 2020; Xia et al., 2022). These gentle inclines are susceptible to the accumulation of groundwater, which facilitates the formation of substantial underground ice and, consequently, slumping. Furthermore, these TSs on the QTP are primarily located on the north and northeast-facing slopes (Xia et al., 2022), which are shaded. The shaded regions experience relatively lower levels of solar radiation, reduced evaporation, and smaller soil pore sizes, all of which promote the development of thick underground ice and create favorable conditions for the emergence of TSs (Lin et al., 2025).

Regarding the TLs, Wei et al. (2021) identified 161,300 TLs with sizes varying from 500 m² to 3 km², encompassing a total area of 2,825.45±5.75 km², as determined through Sentinel-2 images. In a similar vein, Luo et al. (2022b) observed a significant increase in TLs on the central QTP, noting a 158% rise in number and a 123% increase in area over the last five decades, based on visual assessments of aerial and satellite images from SPOT-5 and Gaofen-1 at high spatial resolution. Traditional threshold-based detection methods often overlook smaller TLs under 500 m² due to the constraints of image spatial resolution (Wei et

https://doi.org/10.5194/egusphere-2025-4184
Preprint. Discussion started: 28 October 2025

al., 2021). Advancements in deep learning have enabled Tian et al. (2024) to enhance their TLs inventory by employing U-Net for water body extraction in the Qilian Mountains. Additionally, Zhang et al. (2024) leveraged ESRI's World Imagery Wayback at a resolution of 1.2 m as the primary input for their improved DeepLabV3+ model, identifying 52,486 TLs in the Yellow River Source region alone. Remarkably, nearly 90.2% of these lakes were smaller than 0.01 km², and about 45% were not included in existing inventories.

On the QTP, over 90% of TLs are in continuous permafrost areas, with around 70% situated at elevations between about 4,500 and 5,000 meters (Wei et al., 2021). TLs can often be found surrounding the existing big lakes (Fig. 10). Additionally, most of these lakes are found near engineering corridors on slopes of less than 3° (Zhou et al., 2024). Geographically, they are concentrated in three primary watersheds: the Inner Plateau Basin, the Yangtze River Basin, and the Yellow River Basin (Wei et al., 2021), where ground ice is relatively plentiful (Zou et al., 2024). In terms of land cover and soil properties, TLs on the QTP are mainly associated with two types of vegetation: alpine swamp meadow and alpine meadow. Both types are characterized by sandy loam soil, which is highly porous and has a limited capacity for water retention (Wei et al., 2021). These environmental conditions suggest that TLs develop through localized and uneven subsidence of ice-rich permafrost, promoting gradual water accumulation. This subsidence subsequently modifies the thermal dynamics of the permafrost, resulting in ongoing lake expansion (Grosse et al., 2013). The thermal dynamics of TLs and their surrounding environment are complex. Initially, TLs cause notable deviations from the established regional ground temperature patterns (Jorgenson et al., 2010). The transfer of heat from water to the permafrost beneath it speeds up the melting of ground ice, which in turn promotes the expansion of TLs and the deepening of taliks (Grosse et al., 2013). Moreover, the growth of TLs necessitates not only heat sources but also specific thermo-triggering events to commence this gradual transformation. This observation is consistent with findings that TLs on the QTP are primarily located in transitional, sub-stable, and relatively warmer permafrost areas, where the mean annual ground temperature (MAGT) can reach -1.5 °C, making them more vulnerable to extreme weather events such as summer heatwaves. Interestingly, increased water input from precipitation can also play a role in the formation and expansion of TLs, further affecting the dynamics of permafrost degradation (Zhou et al., 2024).

The railway and highway systems over the QTEC largely overlap in our study area from Lhasa to Golmud (Fig. 1). Both types of roads show an upward trend in the number of TSs and TLs as the buffer distance increases, with a particularly noticeable rise in TLs. The count of TSs varies between 8 and 18 for both road types, whereas TLs are consistently more numerous in the buffer zones of national highways, ranging from 821 to 2,812, compared to 503 to 1,736 for railway buffer zones. Specifically, TSs begin at the same number (8) within a 500 m buffer for both road types, while the TLs for the national highway buffer (821) exceed those for the railway buffer (503). As the buffer extends to 1,000 m, TSs increase to 11 for railways and 14 for national highways, with an enlarged difference in TLs (958 vs. 1,401). At a 1,500 m buffer, TSs rise to 15 for railways and 17 for national highways, while the disparity in TLs continues to grow (1,349 vs. 2,113). By the time the buffer reaches 2,000 m, TSs peak at 18, but TLs remain significantly higher for national highways (2,812 vs. 1,736).

https://doi.org/10.5194/egusphere-2025-4184
Preprint. Discussion started: 28 October 2025

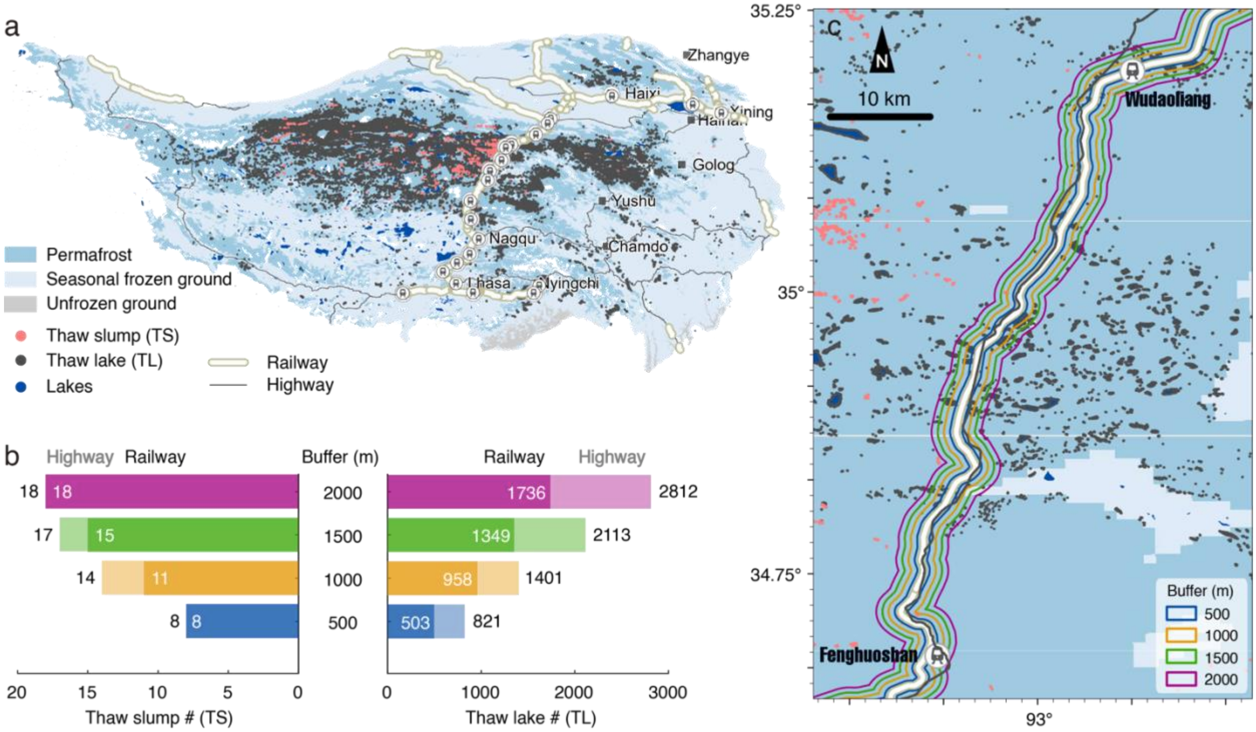

Figure 10: The thaw slump (TS) and thermokarst/thaw lake (TL). a, the spatial distribution of TSs and TLs over QTP. b, the number of TSs and TLs in the given buffers from 500 to 2000 meters of the railway and highway systems of QTEC. c, an enlarged view from Fenghuoshan to Wudaoliang railway stations over the QTEC.

4.4 Risks mitigation due to permafrost thaw

Climate change poses significant risks to the engineering integrity of infrastructures constructed on permafrost landscape globally. Melvin et al. (2016) assessed the potential economic losses to Alaska's public infrastructure resulting from climate change-induced floods, precipitation, thawing of near-surface permafrost, and frost-heave, thaw-settlement cycles. The authors noted that, in the absence of adaptation, climate-related infrastructure damages between 2015 and 2099 would accumulate to 4.2 billion and 5.5 billion U.S. dollars under Representative Concentration Pathway (RCP) 4.5 and RCP 8.5 scenarios, respectively. The most significant losses are attributed to road flooding due to increased precipitation, followed by damage to buildings associated with the thawing of near-surface permafrost. Hjort et al. (2018) developed geological hazard indices based on the projection of future ground thermal conditions. Their findings indicate that by 2050, approximately four million people—representing about 75% of the present-day population residing in permafrost regions of the Northern Hemisphere—along with around 70% of infrastructure, including residential, transportation, and industrial facilities, will face a heightened risk of near-surface permafrost melting. Additionally, one-third of the infrastructure across the pan-Arctic and 45% of

https://doi.org/10.5194/egusphere-2025-4184
Preprint. Discussion started: 28 October 2025

hydrocarbon extraction sites in the Russian Arctic are situated in areas vulnerable to significant damage from ground instability caused by melting. Notably, even if the goals of the Paris Agreement are achieved, the risks associated with permafrost degradation to infrastructure will remain largely unmitigated.

On the QTP, the subsidence of permafrost and its associated hazards have resulted in significant damage to infrastructure, including roads, power transmission lines, and oil pipelines. The QTEC, which stretches approximately 550 km between Xidatan and Nagqu, traverses a permafrost zone that varies in width from hundreds to thousands of meters. This north-south corridor hosts major projects such as the Qinghai-Tibet highway and railway, the Golmud-Lhasa oil pipeline, the Lanzhou-Xining-Lahsa optical fiber cable, and high-voltage transmission lines, serving as a vital connection between the plains and the QTP regions. Permafrost thawing poses a significant risk to the structural integrity of the engineering infrastructure of QTEC. Evidence of the settling of embankments along the Qinghai-Tibet Highway and Railway, the formation of cracks and potholes on road surfaces, the subsidence of transmission towers, and the erosion of oil pipelines has been identified (Chai et al., 2018; Guo et al., 2016; Sun et al., 2024; Yu et al., 2016). The essential aspect of hazard mitigation involves maintaining the coolness of permafrost through the management of heat convection, solar radiation, and conduction (Wu et al., 2024).

Ran et al. (2022) assessed the mean annual ground temperature and the active layer thickness in the conditions of various shared socioeconomic pathways (SSPs). The authors compiled multiple hazard indices to evaluate the potential degradation of permafrost in the future. Utilizing a lifespan replacement model, the authors estimated the future costs associated with the diminished lifespan of infrastructure. Their findings indicated that by 2090, under the SSP2-4.5 scenario, an additional expenditure of approximately 6.31 billion Chinese Yuan would be necessary to sustain the operational functions of existing infrastructure. Furthermore, the process of engineering construction may also impact the soil's thermo-hydro-mechanical properties in permafrost regions, potentially compromising the stability of permafrost and undermining the integrity of engineering structures.

5 Conclusion

QTEC supports critical lifelines and has strategic significance for the nation. Here, the railways and highways were built atop the permafrost that is highly sensitive to climate change. In this study, we generate time-series ground displacement data from 2014 to 2022 using ascending and descending observations from the Copernicus Sentinel-1 mission. We separated secular deformation trends from seasonal signals, quantified seasonal amplitudes and timing, and inferred motion directions by leveraging the complementary viewing geometries of the satellite orbits. Our findings reveal widespread land subsidence across the QTEC, with deformation rates ranging from a few to over 20 mm/year, especially pronounced between Golmud and Nagqu. Seasonal ground movements on valley floors closely track ground temperature cycles, with maximum uplift typically occurring in spring. In contrast, some hillslopes experience peak uplift in fall, likely due to delayed elastic rebound following

https://doi.org/10.5194/egusphere-2025-4184
Preprint. Discussion started: 28 October 2025

meltwater drainage. Estimates of ALT remain uncertain across studies and methods. However, seasonal vertical displacement amplitude provides a useful lower-bound constraint: areas showing amplitudes larger than 55 mm likely have ALTs of at least 1 m. Applying the constraint from in-situ ALT measurements and the assumption about the ice melts out in the active layer during the thaw season, the freeze–thaw density-change theory allows us to construct a high-resolution regional map of ALT estimates. Finally, we compile inventories of thermokarst disasters adjacent to QTEC infrastructure. Within a 2-km buffer along highways between Lhasa and Golmud, we locate 18 thermokarst/thaw slumps and 2,812 thaw lakes. The growing occurrence of ground deformation and thermokarst activity presents significant risks to environmental stability and infrastructure integrity. Addressing these challenges in QTEC requires integrated scientific assessments and engineering interventions to enhance resilience in the face of ongoing climate change.

Data availability statement. The permafrost distribution map is from Zou et al. (2017) at doi:10.5194/tc-11-2527-2017. The Sentinel-1 data are available from the Copernicus at https://browser.dataspace.copernicus.eu/. Active layer thickness estimates are available from Ni et al. (2021) at doi:10.1029/2020JD033402 and Niu and Yin (2018) archived in the National Tibetan Plateau / Third Pole Environment Data Center at doi:10.11888/GlaciolGeocryol.tpe.0000079.file and https://cstr.cn/18406.11.GlaciolGeocryol.tpe.0000079.file. In-situ ALT measurements are available from Chang et al. (2024) and references therein at doi:10.1038/s41612-024-00866-0, in which the ones used in this study is available in the Supplementary Table. Ground temperature data are available from GLDAS Soil Land Surface (GLDAS2) products at https://disc.gsfc.nasa.gov/datasets/GLDAS_NOAH025_M_2.1/summary?keywords=GLDAS. The soil moisture data estimated from the Soil Moisture Active Passive (SMAP) radiometer observations are extracted from Google Earth Engine at https://developers.google.com/earth-engine/datasets/catalog/NASA_SMAP_SPL4SMGP_007. Our derived estimates of active layer thickness are now archived in our university's online disk (https://disk.pku.edu.cn/link/AA8C7EEB2BD7CB4DB9BA681C415E29E79B) and will be available in Zotero with a digital object identifiers (DOI) when the review procedures being completed.

Author contributions. XH conceptualized and developed the methodology of this this research. XH, YS, SM, YL, YZ, and MC were responsible for data curation and validation. XH, QW, DL, SQ, and KT conducted the investigation. XH drafted the original manuscript with the inputs from all authors.

Competing interests. The authors declare that they have no conflict of interest.

Acknowledgments. ISCE, MintPy, MATLAB, ArcGIS and Adobe Illustrator software programs were applied to compile results and generate figures.

https://doi.org/10.5194/egusphere-2025-4184
Preprint. Discussion started: 28 October 2025

Financial support. This research is financially supported by the National Natural Science Foundation of China (42371078), the Emerging Engineering Interdisciplinary Youth Program at Peking University, the Fundamental Research Funds for the Central Universities, Program of the State Key Laboratory of Cryospheric Science and Frozen Soil Engineering, Northwest Institute of Eco-Environment and Resources, Chinese Academy of Sciences (CSFSE-KF-2414).

References

Berardino, P., Fornaro, G., Lanari, R., and Sansosti, E: A new algorithm for surface deformation monitoring based on small baseline differential SAR interferograms. IEEE Transactions on Geoscience and Remote Sensing, 40(11), 2375–2383, doi:10.1109/tgrs.2002.803792, 2002.

Brown, J., Hinkel, K. M. and Nelson, F. E: The circumpolar active layer monitoring (calm) program: Research designs and initial results 1. Polar Geogr., 24, 166–258, 2000.

Chai, M., Mu, Y., Zhang, J., Ma, W., Liu, G., and Chen, J: Characteristics of asphalt pavement damage in degrading permafrost regions: case study of the Qinghai–Tibet Highway, China. Journal of Cold Regions Engineering, 32(2), doi:10.1061/(asce)cr.1943-5495.0000165, 2018

Chang, T., Yi, Y., Jiang, H., Li, R., Lu, P., Liu, L., Wang, L., Zhao, L., Zwieback, S., and Zhao, J: Unraveling the non-linear relationship between seasonal deformation and permafrost active layer thickness. npj Climate and Atmospheric Science, 7, 308, doi:10.1038/s41612-024-00866-0, 2024.

Chen, J., Wu, T., Zou, D., Liu, L., Wu, X., Gong, W., Zhu, X., Li, R., Hao, J., Hu, G., Pang, Q., Zhang, J., and Yang, S: Magnitudes and patterns of large-scale permafrost ground deformation revealed by Sentinel-1 InSAR on the central Qinghai-Tibet Plateau. Remote Sensing of Environment, 268, 112778, doi:10.1016/j.rse.2021.112778, 2021.

Chen, J., Wu, Y., O'Connor, M., Cardenas, M. B., Schaefer, K., Michaelides, R., and Kling, G: Active layer freeze-thaw and water storage dynamics in permafrost environments inferred from InSAR. Remote Sensing of Environment, 248, 112007, doi:10.1016/j.rse.2020.112007, 2020.

Daout, S., Doin, M., Peltzer, G., Socquet, A., and Lasserre, C: Large-scale InSAR monitoring of permafrost freeze-thaw cycles on the Tibetan Plateau. Geophysical Research Letters, 44(2), 901–909, doi:10.1002/2016gl070781, 2017.

Du, E., Wang, L., Zhao, L., Zhou, H., Liu, S., Zou, D., Liu, G., Xiao, Y., Hu, G., Li, Z., Gao, J., Wang, C., Wang, Y., Wang, X., Chen, W: Quantifying the soil water content of the permafrost active layer using InSAR deformation. Journal of Hydrology, 661, Part B, 133660, 2025.

Ferretti, A., Prati, C., and Rocca, F: Permanent scatterers in SAR interferometry. IEEE Transactions on Geoscience and Remote Sensing, 39(1), 8–20, doi:10.1109/36.898661, 2001.

French, H. M:.The periglacial environment (3rd ed.). John Wiley, doi:10.1002/9781118684931, 2007.

Grosse, G., Jones, B., and Arp, C: Thermokarst lakes, drainage, and drained basins. Elsevier, doi:10.1016/b978-0-12-374739-6.00216-5, 2013.

Guo, L., Xie, Y., Yu, Q., You, Y., Wang, X., and Li, X: Displacements of tower foundations in permafrost regions along the Qinghai–Tibet Power Transmission Line. Cold Regions Science and Technology, 121, 187–195, doi:10.1016/j.coldregions.2015.07.012, 2015.

Hjort, J., Karjalainen, O., Aalto, J., Westermann, S., Romanovsky, V. E., Nelson, F. E., Etzelmüller, B., and Luoto, M: Degrading permafrost puts Arctic infrastructure at risk by mid-century. Nature Communications, 9(1), doi:10.1038/s41467-018-07557-4, 2018.

Hjort, J., Streletskiy, D., Doré, G., Wu, Q., Bjella, K., and Luoto, M: Impacts of permafrost degradation on infrastructure. Nature Reviews Earth and Environment, 3(1), 24–38, 2024.

Hu, X., and Bürgmann, R: Aquifer deformation and active faulting in Salt Lake Valley, Utah, USA. Earth and Planetary Science Letters, 547, 116471, doi:10.1016/j.epsl.2020.116471, 2020.

Hu, X., Bürgmann, R., Xu, X., Fielding, E., and Liu, Z: Machine-Learning characterization of tectonic, hydrological and anthropogenic sources of active ground deformation in California. Journal of Geophysical Research Solid Earth, 126(11), doi:10.1029/2021jb022373, 2021.

https://doi.org/10.5194/egusphere-2025-4184
Preprint. Discussion started: 28 October 2025

Hu, X., Lu, Z., and Wang, T: Characterization of Hydrogeological Properties in Salt Lake Valley, Utah, using InSAR. Journal of Geophysical Research Earth Surface, 123(6), 1257–1271, doi:10.1029/2017jf004497, 2018.

Huang, L., Luo, J., Lin, Z., Niu, F., and Liu, L: Using deep learning to map retrogressive thaw slumps in the Beiluhe region (Tibetan Plateau) from CubeSat images. Remote Sensing of Environment, 237, 111534, doi:10.1016/j.rse.2019.111534, 2019.

Jolivet, R., Grandin, R., Lasserre, C., Doin, M.-P., and Peltzer, G: Systematic InSAR tropospheric phase delay corrections from global meteorological reanalysis data. Geophysical Research Letters, 38, 17, L17311, 2011.

Jorgenson, M. T., Romanovsky, V., Harden, J., Shur, Y., O'Donnell, J., Schuur, E. a. G., Kanevskiy, M., and Marchenko, S: Resilience and vulnerability of permafrost to climate change. This article is one of a selection of papers from The Dynamics of Change in Alaska's Boreal Forests: Resilience and Vulnerability in Response to Climate Warming. Canadian Journal of Forest Research, 40(7), 1219–1236, doi:10.1139/x10-060, 2010.

Li, J., Wang, Q., Zhang, Y., Yang, S., and Gao, G: An improved active layer thickness retrieval method over Qinghai-Tibet permafrost using InSAR technology: With emphasis on two-dimensional deformation and unfrozen water. International Journal of Applied Earth Observation and Geoinformation, 124, 103530, doi:10.1016/j.jag.2023.103530, 2023.

Li, R., Zhao, L., Ding, Y., Wu, T., Xiao, Y., Du, E., Liu, G., and Qiao, Y: Temporal and spatial variations of the active layer along the Qinghai-Tibet Highway in a permafrost region. Chinese Science Bulletin, 57(30), 2864-2871, 2012.

Li, Z., Zhao, R., Hu, J., Wen, L., Feng, G., Zhang, Z., and Wang, Q: InSAR analysis of surface deformation over permafrost to estimate active layer thickness based on one-dimensional heat transfer model of soils. Scientific Reports, 5(1), doi:10.1038/srep15542, 2015

Lin, Y., Hu, X., Lu, H., Niu, F., Liu, G., Zhang, L., Zhang, S., Zhang, S., Liu, J., and Liu, Y: Multi-annual inventorying of retrogressive thaw slumps using domain adaptation. Journal of Geophysical Research: Machine Learning and Computation, 2(1). e2024JH000370, 2025.

Liu, L., Schaefer, K., Zhang, T., and Wahr, J: Estimating 1992–2000 average active layer thickness on the Alaskan North Slope from remotely sensed surface subsidence. Journal of Geophysical Research Atmospheres, 117(F01005), doi:10.1029/2011jf002041, 2012.

Liu, L., Zhang, T., and Wahr, J: InSAR measurements of surface deformation over permafrost on the North Slope of Alaska. Journal of Geophysical Research Atmospheres, 115(F3), doi:10.1029/2009jf001547, 2010.

Lu, P., Han, J., Yi, Y., Hao, T., Zhou, F., Meng, X., Zhang, Y., and Li, R: MT-INSAR unveils dynamic permafrost disturbances in Hoh Xil (Kekexili) on the Tibetan Plateau hinterland. IEEE Transactions on Geoscience and Remote Sensing, 61, 1–16, doi:10.1109/tgrs.2023.3253937, 2023.

Lu, Z., and Dzurisin, D: InSAR Imaging of Aleutian Volcanoes: Monitoring a Volcanic Arc from Space. Springer. http://link.springer.com/book/10.1007%2F978-3-642-00348-6, 2014.

Luo, J., Niu, F., Lin, Z., Liu, M., and Yin, G: Development of thawing hazards and thermal influence on permafrost along Qinghai-Tibet Engineering Corridor. Journal of Engineering Geology, 22(2), 326–333, 2014.

Luo, J., Niu, F., Lin, Z., Liu, M., and Yin, G: Recent acceleration of thaw slumping in permafrost terrain of Qinghai-Tibet Plateau: An example from the Beiluhe Region. Geomorphology, 341, 79–85, doi:10.1016/j.geomorph.2019.05.020, 2019.

Luo, J., Niu, F., Lin, Z., Liu, M., Yin, G., and Gao, Z: Abrupt increase in thermokarst lakes on the central Tibetan Plateau over the last 50 years. CATENA, 217, 106497, doi:10.1016/j.catena.2022.106497, 2022a.

Luo, J., Niu, F., Lin, Z., Liu, M., Yin, G., and Gao, Z: Inventory and frequency of retrogressive thaw slumps in permafrost region of the Qinghai–Tibet plateau. Geophysical Research Letters, 49(23), doi:10.1029/2022gl099829, 2022b.

Melvin, A. M., Larsen, P., Boehlert, B., Neumann, J. E., Chinowsky, P., Espinet, X., Martinich, J., Baumann, M. S., Rennels, L., Bothner, A., Nicolsky, D. J., and Marchenko, S. S: Climate change damages to Alaska public infrastructure and the economics of proactive adaptation. Proceedings of the National Academy of Sciences, 114(2), doi:10.1073/pnas.1611056113, 2016.

Mu, C., Shang, J., Zhang, T., Fan, C., Wang, S., Peng, X., Zhong, W., Zhang, F., Mu, M., and Jia, L: Acceleration of thaw slump during 1997–2017 in the Qilian Mountains of the northern Qinghai-Tibetan plateau. Landslides, 17(5), 1051–1062, doi:10.1007/s10346-020-01344-3, 2020.

Nelson, F. E., Anisimov, O. A., and Shiklomanov, N. I: Subsidence risk from thawing permafrost. Nature, 410(6831), 889–890, doi:10.1038/35073746, 2001.

Ni, J., Wu, T., Zhu, X., Hu, G., Zou, D., Wu, X., Li, R., Xie, C., Qiao, Y., Pang, Q., Hao, J., and Yang, C: Simulation of the present and future projection of permafrost on the Qinghai-Tibet Plateau with statistical and machine learning models. Journal of Geophysical Research Atmospheres, 126(2), doi:10.1029/2020jd033402, 2020.

Niu, F., and Yin, G: The active layer depth distribution map of the Qinghai-Tibet Engineering Corridor (1980-2015). [Dataset]. In *National Tibetan Plateau / Third Pole Environment Data Center.* https://data.tpdc.ac.cn/en/data/b38e8767-928d-41f8-a9df-23d50170952c, 2017.

O'Neill, P. E., Chan, S., Njoku, E. G., Jackson, T., Bindlish, R., Chaubell, J. and Colliander, A: SMAP Enhanced L3 Radiometer Global and Polar Grid Daily 9 km EASE-Grid Soil Moisture: SPL3SMP_E, Version 6). [Data Set]. Boulder, Colorado USA. NASA National Snow and Ice Data Center Distributed Active Archive Center, doi:10.5067/M20OXIZHY3RJ, date Accessed 04-30-2025, 2023.

Overeem, I., Jafarov, E., Wang, K., Schaefer, K., Stewart, S., Clow, G., Piper, M., and Elshorbany, Y: A Modeling Toolbox for Permafrost Landscapes. Eos, Transactions of the American Geophysical Union (Online), doi:10.1029/2018EO105155, 2018.

Qu, F., Lu, Z., Kim, J., and Turco, M. J: Mapping and characterizing land deformation during 2007–2011 over the Gulf Coast by L-band InSAR. Remote Sensing of Environment, 284, 113342, doi:10.1016/j.rse.2022.113342, 2022.

Ran, Y., Cheng, G., Dong, Y., Hjort, J., Lovecraft, A. L., Kang, S., Tan, M., and Li, X: Permafrost degradation increases risk and large future costs of infrastructure on the Third Pole. Communications Earth and Environment, 3(1), doi:10.1038/s43247-022-00568-6, 2022.

Ran, Y., Li, X., and Cheng, G.: Climate warming over the past half century has led to thermal degradation of permafrost on the Qinghai–Tibet Plateau, The Cryosphere, 12, 595–608, https://doi.org/10.5194/tc-12-595-2018, 2018.

Reinosch, E., Buckel, J., Dong, J., Gerke, M., Baade, J., and Riedel, B: InSAR time series analysis of seasonal surface displacement dynamics on the Tibetan Plateau. The Cryosphere, 14(5), 1633–1650, doi:10.5194/tc-14-1633-2020, 2020.

Rouyet, L., Lauknes, T. R., Christiansen, H. H., Strand, S. M., and Larsen, Y: Seasonal dynamics of a permafrost landscape, Adventdalen, Svalbard, investigated by InSAR. Remote Sensing of Environment, 231, 111236, doi:10.1016/j.rse.2019.111236, 2019.

Rudy, A. C., Lamoureux, S. F., Treitz, P., Short, N., and Brisco, B: Seasonal and multi-year surface displacements measured by DInSAR in a High Arctic permafrost environment. International Journal of Applied Earth Observation and Geoinformation, 64, 51–61, doi:10.1016/j.jag.2017.09.002, 2017.

Harris, S. A., French, H. M., Heginbottom, J. A., Johnston, G. H., Ladanyi, B., Sego, D. C., van Everdingen, R. O: Glossary of permafrost and related ground-ice terms. In Arctic and Alpine Research. Associate Committee on Geotechnical Research, National Research Council of Canada, 1988.

Sun, Z., Ma, W., Li, G., Liu, Y., and Wu, G: Degrading permafrost beneath road embankments of the Qinghai-Tibet Highway from 1995 to 2020. Cold Regions Science and Technology, 219, 104133, doi:10.1016/j.coldregions.2024.104133, 2024.

Tian, W., Peng, X., Frauenfeld, O. W., Weisai, L., Wei, G., Chen, G., and Huang, Y: A new inventory and future projections of thermokarst lakes in the permafrost regions of the Qilian Mountains, northeastern Qinghai-Tibet Plateau, China. Geomorphology, 462, 109348, doi:10.1016/j.geomorph.2024.109348, 2024.

Wang, C., Zhang, Z., Zhang, H., Zhang, B., Tang, Y., and Wu, Q: Active layer thickness retrieval of Qinghai–Tibet permafrost using the TerraSAR-X InSAR technique. IEEE Journal of Selected Topics in Applied Earth Observations and Remote Sensing, 11(11), 4403–4413, doi:10.1109/jstars.2018.2873219, 2018.

Wei, Z., Du, Z., Wang, L., Lin, J., Feng, Y., Xu, Q., and Xiao, C: Sentinel-based inventory of thermokarst lakes and ponds across permafrost landscapes on the Qinghai-Tibet plateau. Earth and Space Science, 8(11), doi:10.1029/2021ea001950, 2021.

Wu, Q., Zhang, T. and Liu, Y: Thermal state of the active layer and permafrost along the Qinghai-Xizang (Tibet) Railway from 2006 to 2010. The Cryosphere, 6, 607–612, 2012.

Wu, Q., Ma, W., Lai, Y., and Cheng, G: Permafrost degradation threatening the Qinghai−Xizang Railway. Engineering, doi:10.1016/j.eng.2024.01.023, 2024.

Xia, Z., Huang, L., Fan, C., Jia, S., Lin, Z., Liu, L., Luo, J., Niu, F., and Zhang, T: Retrogressive thaw slumps along the Qinghai–Tibet Engineering Corridor: a comprehensive inventory and their distribution characteristics. Earth System Science Data, 14(9), 3875–3887, doi:10.5194/essd-14-3875-2022, 2022.

Yin, G., Zheng, H., Niu, F., Luo, J., Lin, Z., and Liu, M: Numerical mapping and modeling permafrost thermal dynamics across the Qinghai-Tibet Engineering Corridor, China integrated with remote sensing. Remote Sensing, 10(12), 2069, doi:10.3390/rs10122069, 2018.

Yu, F., Qi, J., Yao, X., and Liu, Y: In-situ monitoring of settlement at different layers under embankments in permafrost regions on the Qinghai–Tibet Plateau. Engineering Geology, 160, 44–53, doi:10.1016/j.enggeo.2013.04.002, 2013.

Zhang, Y., Fattahi, H., and Amelung, F: Small baseline InSAR time series analysis: Unwrapping error correction and noise reduction. Comput. Geosci., 133, 104331, 2019.

Zhang, K., Feng, M., Sui, Y., Xu, J., Yan, D., Hu, Z., Han, F., and Sthapit, E: Identifying thermokarst lakes using deep learning and high-resolution satellite images. Science of Remote Sensing, 10, 100175, doi:10.1016/j.srs.2024.100175, 2024.

Zhang, Z., and Wu, Q: Predicting Changes of Active Layer Thickness on the Qinghai-Tibet Plateau as Climate Warming. Journal of Glaciology and Geocryology, in Chinese, 34(3), 505–511, 2012.

Zhang, X., Zhang, H., Wang, C., Tang, Y., Zhang, B., Wu, F., Wang, J., and Zhang, Z: Active layer thickness retrieval over the Qinghai-Tibet plateau using Sentinel-1 multitemporal InSAR monitored permafrost subsidence and temporal-spatial multilayer soil moisture data. IEEE Access, 8, 84336–84351, doi:10.1109/access.2020.2988482, 2020.

Zhao, L., Zou, D., Hu, G., Wu, T., Du, E., Liu, G., Xiao, Y., Li, R., Pang, Q., Qiao, Y., Wu, X., Sun, Z., Xing, Z., Sheng, Y., Zhao, Y., Shi, J., Xie, C., Wang, L., Wang, C., and Cheng, G: A synthesis dataset of permafrost thermal state for the Qinghai–Tibet (Xizang) Plateau, China. Earth System Science Data, 13(8), 4207–4218, doi:10.5194/essd-13-4207-2021, 2021.

Zhao, L., Zou, D., Hu, G., Du, E., Pang, Q., Xiao, Y., Li, R., Sheng, Y., Wu, X., Sun, Z., Wang, L., Wang, C., Ma, L., Zhou, H., and Liu, S: Changing climate and the permafrost environment on the Qinghai–Tibet (Xizang) plateau. Permafrost and Periglacial Process, 31, 396–405, 2020.

Zhao, Y., Nan, Z., Ji, H., and Zhao, L: Convective heat transfer of spring meltwater accelerates active layer phase change in Tibet permafrost areas. The Cryosphere, 16(3), 825–849, doi:10.5194/tc-16-825-2022, 2022.

Zheng, W., Hu, J., Lu, Z., Hu, X., Sun, Q., Liu, J., Zhu, J., and Li, Z: Enhanced kinematic inversion of 3-D displacements, geometry, and hydraulic properties of a North-South slow-moving landslide in three gorges reservoir. Journal of Geophysical Research Solid Earth, 128(6), doi:10.1029/2022jb026232, 2023.

Zhou, G., Liu, W., Xie, C., Song, X., Zhang, Q., Li, Q., Liu, G., Li, Q., and Luo, B: Accelerating thermokarst lake changes on the Qinghai–Tibetan Plateau. Scientific Reports, 14(1), doi:10.1038/s41598-024-52558-7, 2024.

Zou, D., Pang, Q., Zhao, L., Wang, L., Hu, G., Du, E., Liu, G., Liu, S., and Liu, Y: Estimation of permafrost ground ice to 10 m depth on the Qinghai-Tibet Plateau. Permafrost and Periglacial Processes, 35(3), 423–434, doi:10.1002/ppp.2226, 2024.Zou, D., Zhao, L., Sheng, Y., Chen, J., Hu, G., Wu, T., Wu, J., Xie, C., Wu, X., Pang, Q., Wang, W., Du, E., Li, W., Liu, G., Li, J., Qin, Y., Qiao, Y., Wang, Z., Shi, J., and Cheng, G.: A new map of permafrost distribution on the Tibetan Plateau, The Cryosphere, 11, 2527–2542, https://doi.org/10.5194/tc-11-2527-2017, 2017.